

Bidirectional reflectance measurements of sediments in the vicinity of Lee Stocking Island, Bahamas

Hao Zhang and Kenneth J. Voss¹

Department of Physics, University of Miami, Coral Gables, Florida 333143

R. Pamela Reid and Eric M. Louchard

Rosenstiel School of Marine and Atmospheric Science, University of Miami, 4600 Rickenbacker Causeway, Miami, Florida 33149

Abstract

In situ measurements of bidirectional reflectance factors (REFFs) are presented for submerged carbonate sediments at six sites in the vicinity of Lee Stocking Island. Sediment grain sizes ranged from 400 μm to $>1000 \mu\text{m}$. Several features were common to all data sets. Although overall sediment reflectance varied spectrally, normalized REFF was independent of wavelength within the natural sample variability. This allowed us to derive a model REFF which, when multiplied by $\text{REFF}(\theta_i = 0^\circ, \theta_r = 45^\circ, \phi)$ at a specific wavelength, represented the data well. In addition, normally illuminated samples were almost Lambertian, but samples with larger grain sizes had an REFF that decreased with increasing view angles. As the illumination angle increased, samples became increasingly non-Lambertian. The dominant feature of the REFF in these non-Lambertian surfaces is in the backscattering direction. In this direction the REFF was significantly larger than the nadir value. The largest backscattering REFFs correspond to large grain sizes and increases with increasing illumination angles. The empirical model, which represents the data within one standard deviation of sample variation, is presented for these sediments. This model is well behaved at angles out to 90° and thus can be used in radiative transfer models. This model provides a realistic bottom reflectance that can be used to improve light field predictions in shallow water.

The bidirectional reflectance distribution function (BRDF) provides a complete description of light reflection from a surface. It describes the variation of reflectance with both incident nadir angle (angle between the surface normal and the incident collimated irradiance) (θ_i); reflected, or view, nadir angle (θ_r); and the azimuthal angle between the incident and reflected light (ϕ). A complete $\text{BRDF}(\theta_i, \theta_r, \phi)$ is the fundamental parameter needed to make an accurate prediction of how light would be reflected from a surface, or in calculating the light field near the surface. Since the reflectance from a surface can be dependent on θ_i , θ_r , and ϕ , numerous measurements are required to experimentally characterize the $\text{BRDF}(\theta_i, \theta_r, \phi)$ of a surface. Because of the difficulty in obtaining a complete suite of measurements, $\text{BRDF}(\theta_i, \theta_r, \phi)$ has not previously been measured in benthic marine environments. In shallow water, most radiative transfer models have either approximated the surface as Lambertian or used a land surface BRDF (Maritorena et al. 1994).

One of the goals of the Coastal Benthic Optical Properties (CoBOP) program is to improve models of the light field near the sediment–water interface. As part of this work, we developed an instrument that allows rapid, accurate measurement of in situ $\text{BRDF}(\theta_i, \theta_r, \phi)$ in the shallow ($<30 \text{ m}$)

coastal environment (Voss et al. 2000). In this paper we discuss the variability of the $\text{BRDF}(\theta_i, \theta_r, \phi)$ in the sediments around Lee Stocking Island. This site is characterized by a variety of distinct sediment types, with grain sizes ranging from 400 μm to $>1,000 \mu\text{m}$. The BRDF meter measures the $\text{BRDF}(\theta_i, \theta_r, \phi)$ in a 3-cm² area. Thus, sample variability must be able to be characterized on this scale, or smaller. This technique is well suited for sediment with grain sizes less than a few millimeters but is not appropriate for coral, pebbles, or plants. All measurements were made on submerged marine sediments.

For use in radiative transfer models, the $\text{BRDF}(\theta_i, \theta_r, \phi)$ must be represented analytically. We chose a relatively simple equation to describe the $\text{BRDF}(\theta_i, \theta_r, \phi)$ of individual sediments, which fit the data within 1 standard deviation (SD) of the variability in the individual samples. This allows the incorporation of realistic BRDF values into an empirical model. This model, however, does not allow full understanding of the relationships between $\text{BRDF}(\theta_i, \theta_r, \phi)$ and the optics of the individual sediment grains. Making this connection will be the topic of future work.

Methods

Instrument description—The BRDF meter and its calibration have been described in detail elsewhere (Voss et al. 2000). The instrument uses fiber-optic cables to collect light from many fixed viewing angles (>100 positions, $5^\circ \leq \theta_r \leq 65^\circ$, $15^\circ \leq \phi \leq 345^\circ$) and to bring this light to a cooled CCD array camera (First Magnitude). Three colors of LED sequentially illuminate other optical fibers to produce collimated irradiance to illuminate the surface. The instrument

¹ Corresponding author (voss@physics.miami.edu).

Acknowledgments

This work was supported by the Ocean Optics program at the Office of Naval Research under grants N000149910008 (K.J.V., H.Z.) and N000149710010 (P.R., E.L.). We also thank the staff of the Caribbean Marine Research Center at Lee Stocking Island, Bahamas, and Albert L. Chapin for their help in collecting the experimental data.

Table 1. Sampling sites and sediment characteristics; est. indicates visual estimate.

Site	Sediment description	Average grain size (μm)	Comments	Number of samples averaged
Horseshoe Reef 1	Skeletal sand, molluscs dominant (est.)	1,000–2,000 (est.)	10-m water depth, large sand waves	5
Norman's Yellow	grapestone sand with thick yellow film	1,100	2-m water depth, yellow algal film on sediment	3
Norman's White	grapestone sand	875	2-m water depth, turbated areas with little algae	4
Ooid Shoal	migrating ooid sand	600	1–2-m water depth, high current, sand waves	4
Horseshoe Reef 2	Skeletal sand, molluscs dominant (est.)	500 (est.)	10-m water depth, grain size varies in sand waves	4
Rainbow South	migrating ooid sand	430	2-m water depth, high current, sand waves	3

incorporates eight different illumination angles (θ_i) ranging from 0 to 65°. All viewing angles for a single color and illumination angle are collected in a single 16-bit camera image. The measurement region of the instrument resembles an overturned bowl (20 cm in diameter), which is open to the external (air or water) environment. A black anodized aluminum strip runs across the instrument opening to orient the instrument with respect to the sample. Because of the measurement geometry, the vertical position of the sample is important for accurate measurement and the correct position is maintained by the aluminum band. The entire instrument can be battery powered, is in an underwater housing, and is self-contained. The instrument can be diver operated, enabling in situ measurements of benthic spectral BRDF(θ_i, θ_r, ϕ).

The data presented are shown as reflectance factors, REFF(θ_i, θ_r, ϕ) (Hapke 1993). The REFF(θ_i, θ_r, ϕ) is the ratio of the measured reflectance in a given direction relative to that of a perfect diffuse (Lambertian) reflector. In these units, a perfect Lambertian reflector (reflectance 1) would have REFF(θ_i, θ_r, ϕ) = 1. This can be simply related to the BRDF as follows: REFF(θ_i, θ_r, ϕ) = π BRDF(θ_i, θ_r, ϕ). This form of data presentation allows easy comparison with the expected REFF, or BRDF, of a Lambertian surface.

The instrument has an estimated precision of 1–2% (based on repeated measurements of a stable sample) and an accuracy of 10%. Calibrations are based on measurements of Spectralon plaques (Labsphere) and are performed in water and in air. A calibration plaque is also taken into the field, and calibrations are performed periodically during the measurement period.

Sample sites and sediment description—In situ measurements of BRDF were made on sediments at six sites (Table 1), which were representative of sediment variability in the vicinity of LSI. These sediments are typical of carbonate sediments throughout the Bahamas and in other shallow tropical locations. Sediment grain composition and grain size were determined for all sites except Horseshoe Reef from two sets of three cores taken using 22-mm diameter, 10-cm long acrylic tubes. Grain size and composition was visually estimated for the Horseshoe reef site. For grain size mea-

surements, sediment from the cores was freeze-dried and sieved with 7.5-cm hand sieves to measure sizes ranging from 2.00 to 4.75 mm. A Coulter LS-200 was used to measure the grain size distribution for grains less than 2.00-mm diameter. Grain composition was analyzed using thin sections from the top 1 cm of sediment cores. Samples were prepared by pushing 1 cm of the core up out of the core tube dry and supported by a ring of acrylic tubing. One cm is sliced off, placed in a butyrate dish, and impregnated with Epotek 301. Samples were examined under an Olympus BH-2 petrographic microscope and photographed with an Olympus DP10 digital camera. Images were then overlaid with a 100- μm grid for point counting of grains larger than 63 μm .

Representative measurements of BRDF were taken from each site by averaging 3–5 measurements. The BRDF meter was rotated or moved to an adjacent spot for each separate measurement. Two of the sites (Norman's Yellow and Norman's White) did not have wave structure on the sediment surface. In these sites the BRDF meter could be placed directly on the surface and the sediment surface normal is parallel with the vertical direction in the water column. For three sites (Horseshoe Reef 1, Horseshoe Reef 2, and Ooid Shoal) there were extensive sand waves on the surface, but the wavelength of these waves was sufficiently long (minimum surface curvature) that the instrument could be placed on the surface; the nadir direction of the instrument was aligned with the local surface normal. For the Horseshoe Reef 2 sample, while the grain size of the sediment varied visually, the BRDF taken at different spots along the sand wave (crest/trough) did not differ more than the deviation between individual samples on the crest or trough. Thus all measurements here were averaged together. For the final sample, Rainbow South, the sediment had large sand waves evident with short wavelengths, but the grain size was very homogenous. Here the surface was artificially flattened, with a swim fin, to obtain a flat surface. In all of these measurements we felt it was most important to make an accurate measurement with respect to the local, well-defined, surface normal. Thus, these measurements, or the model derived from them, could be used in other models that have variations in bottom topography (such as Zaneveld and Boss

2003; Mobley and Sundman 2003; and Carder et al. 2003) to give the BRDF for a larger surface area.

Experimental results

Sediment REFF—To illustrate the variation of measured REFF values, results for sediments from two sites (Rainbow South and Norman's Yellow), which illustrate extremes in measured values, are discussed in detail. As will be emphasized in a later section, $REFF(\theta_i, \theta_r, \phi)$ measured for single samples at multiple wavelengths show no statistically significant differences when normalized by factors such as the normally illuminated surface albedo, or $REFF(0^\circ, 45^\circ, \phi)$. Hence we present only measurements in the red wavelength. The $REFF(\theta_i, \theta_r, \phi)$ for sediments at the other sites have features similar to the sediments at Norman's Yellow and Rainbow South.

(i) **Rainbow South**—Figure 1 shows the $REFF(\theta_i, \theta_r, \phi)$ factor for the Rainbow South sample at 640 nm and two illumination angles, 0° and 65° . These are the two extreme illumination angles measured. Many of the features common to all the natural samples we measured are exhibited in these two contour plots.

Figure 1A is the $REFF(\theta_i = 0^\circ, \theta_r, \phi)$. The layout of the graph will be similar for all the contour plots shown in the paper. The center (0, 0) represents light coming perpendicular to the surface. The nadir angle is linearly proportional to the distance from the center. ϕ is arranged such that 0° , measured from the source of the illumination, is in the top center of the graph. Light reflected back toward the source would be represented toward the top of this graph. Light that has been reflected in the forward direction (such as a mirror would send light) is toward the bottom of the graph. The left and right side of the images should be symmetric for a perfect surface, but with real data they are often not exactly symmetric. The plus signs in the plot show where the measurement viewing locations, upon which the contour graph has been based, are in the geometry. They are distributed throughout the left and right side of the coordinate system, giving a measure of surface symmetry. The measurements are also concentrated in the forward (specular) and backward ("hotspot") directions, as these are often areas of rapid change in natural samples. These viewing locations are fixed and constant for each measurement, and thus are not shown in later graphs. The illumination angle changes as a different illumination fiber is illuminated and illumination color is varied by turning on another LED color. Also note that the maximum nadir angle for viewing and illumination is 65° ; hence the data/contours stop at this angle.

The contour lines in most of the figures are at 0.04 in reflectance factor. In Fig. 1A it can be seen that there are very few contour lines. This illustrates an important characteristic of many of our samples, for normal illumination the samples tend to be nearly Lambertian. This sample is within ± 0.04 reflectance units (less than 10%) of being perfectly Lambertian. This implies that the assumption of a Lambertian reflector is relatively good, as long as the surface is illuminated at, or near, the normal direction.

Figure 1B is for the same surface and color as Fig. 1A,

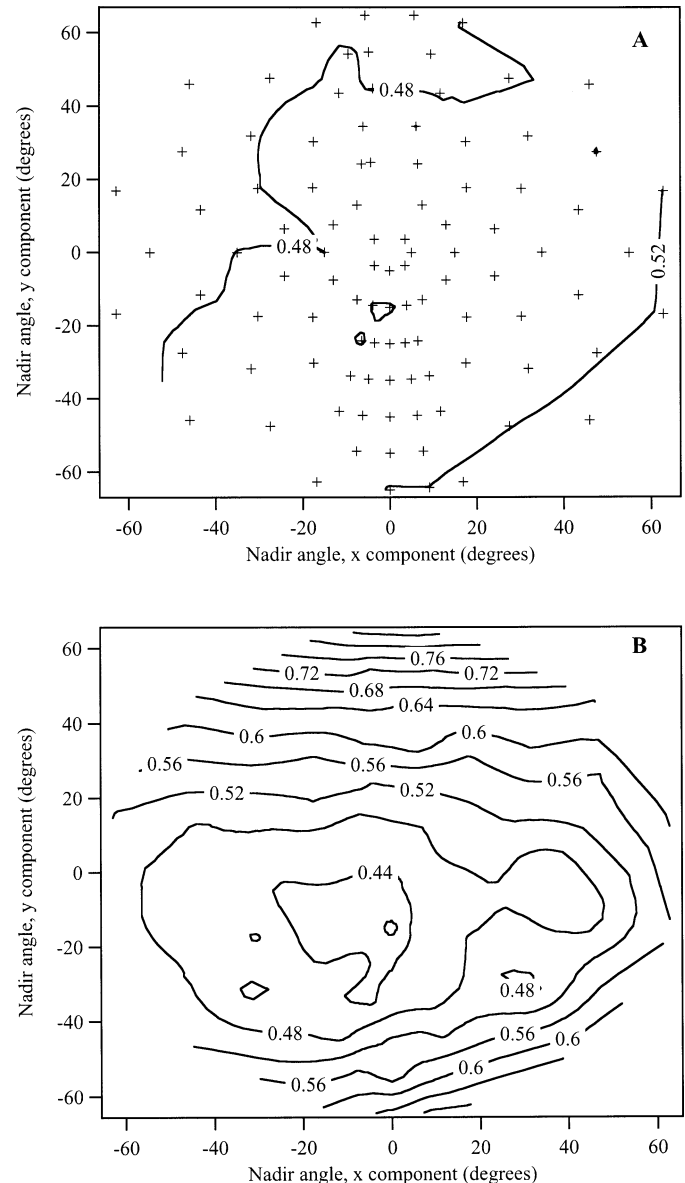


Fig. 1. $REFF(\theta_i, \theta_r, \phi)$ for the Rainbow South sample, at 640 nm, and two illumination angles, (A) 0° and (B) 65° . The plus signs in (A) show the measurement viewing angles. The center (0, 0) represents light that would be coming directly up at nadir. The nadir angle is linearly proportional to distance from the center. ϕ is arranged such that 0° , measured from the source of the illumination, is in the top center of the graph. Light reflected back toward the source would be represented toward the top of this graph. Light that has been reflected in the forward direction (such as a mirror would send light) is toward the bottom of the graph. Contour lines are at every 0.04 in REFF.

but in this case $\theta_i = 65^\circ$. This sample shows two non-Lambertian effects. The first, and most common throughout all of our natural samples, is that there is a hotspot or enhanced reflectance in the backward direction (toward the top). This is common in almost all natural surfaces that have surface texture. This enhancement is caused by the lack of shadows if one looks along the direction of illumination relative to

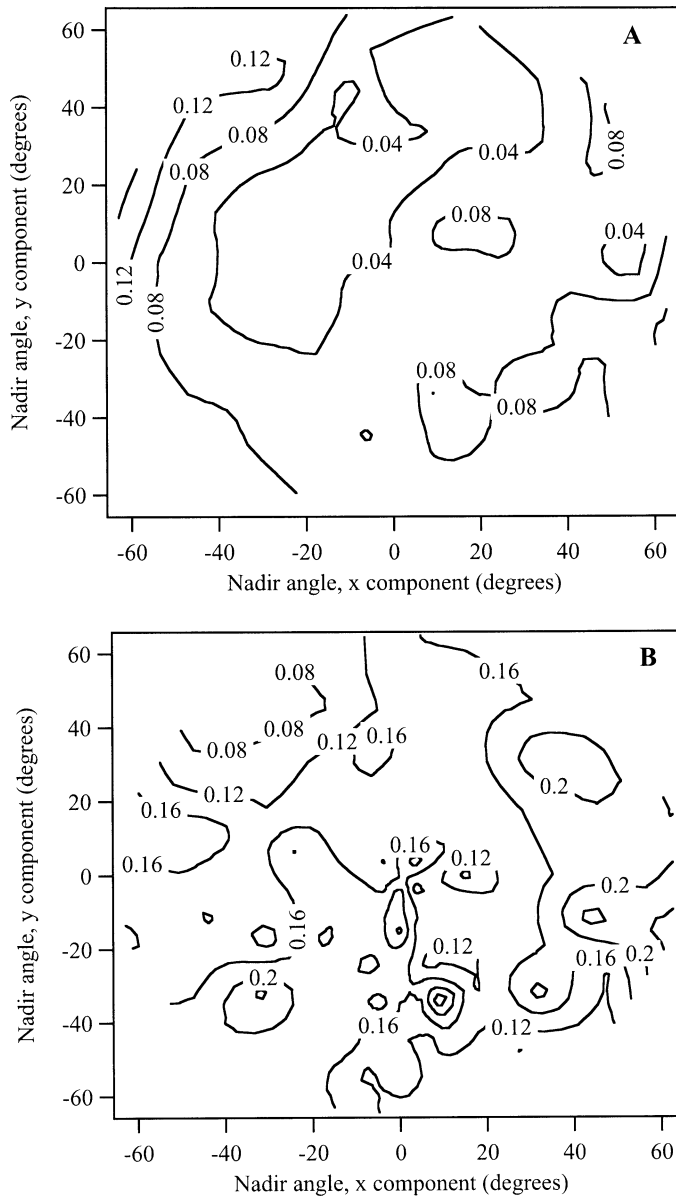


Fig. 2. Normalized standard deviation of the samples used to construct the Rainbow South average. (A) $\theta_i = 0^\circ$, (B) $\theta_i = 65^\circ$.

other viewing angles. The other feature evident in this figure is the enhancement in forward, or specular, reflectance. This is not a common feature in most of the samples we have measured, but it is obvious in this sample. It also appears in some of the artificial surfaces, such as spectralon (McGuckin et al. 1997). In this case the hotspot is responsible for an enhancement of the reflectance of a factor of 2 between the hotspot and nadir, while the specular component is a 50% enhancement between the nadir and the specular maximum.

Figure 2 shows the normalized standard deviation between the samples averaged to obtain Fig. 1. For $\theta_i = 0^\circ$ (Fig. 2A), the standard deviation between the samples is small, mostly less than 10%. This is a combination of measurement precision (for a very uniform, homogeneous surface the error in precision is less than 1%), sample variability, and sample

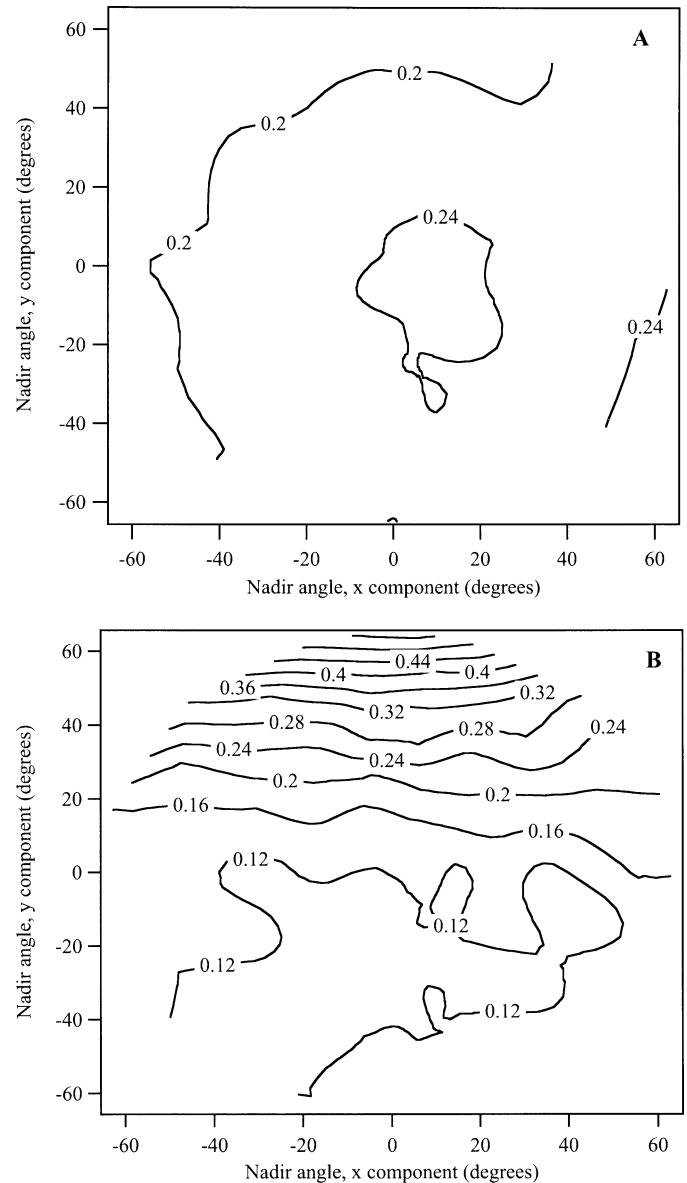


Fig. 3. $REFF(\theta_i, \theta_r, \phi)$ for the Norman's Yellow sample, at 640 nm, and two illumination angles, (A) 0° and (B) 65° .

measurement conditions (sample height, residual slope). Even for $\theta_i = 65^\circ$ (Fig. 2B) the standard deviation is less than 20%. Thus these data are a very good representation of the Rainbow South $REFF(\theta_i, \theta_r, \phi)$.

(ii) *Norman's Yellow*—The other end of the measured size spectrum (large particles) is Norman's Yellow. A contour plot of the $REFF(\theta_i, \theta_r, \phi)$ for this sample is shown in Fig. 3. In the normally illuminated case (Fig. 3A), the first contrast with Rainbow South is the much lower overall reflectance. This sample was darker than the Rainbow South, and as can be seen, the $REFF(\theta_i, \theta_r, \phi)$ is less than half as large. The next difference between the two samples is that the $REFF(\theta_i, \theta_r, \phi)$ is somewhat less Lambertian, even for normally illuminated light. As the sample grain size increased there was a tendency for the $REFF(\theta_i, \theta_r, \phi)$ to decrease

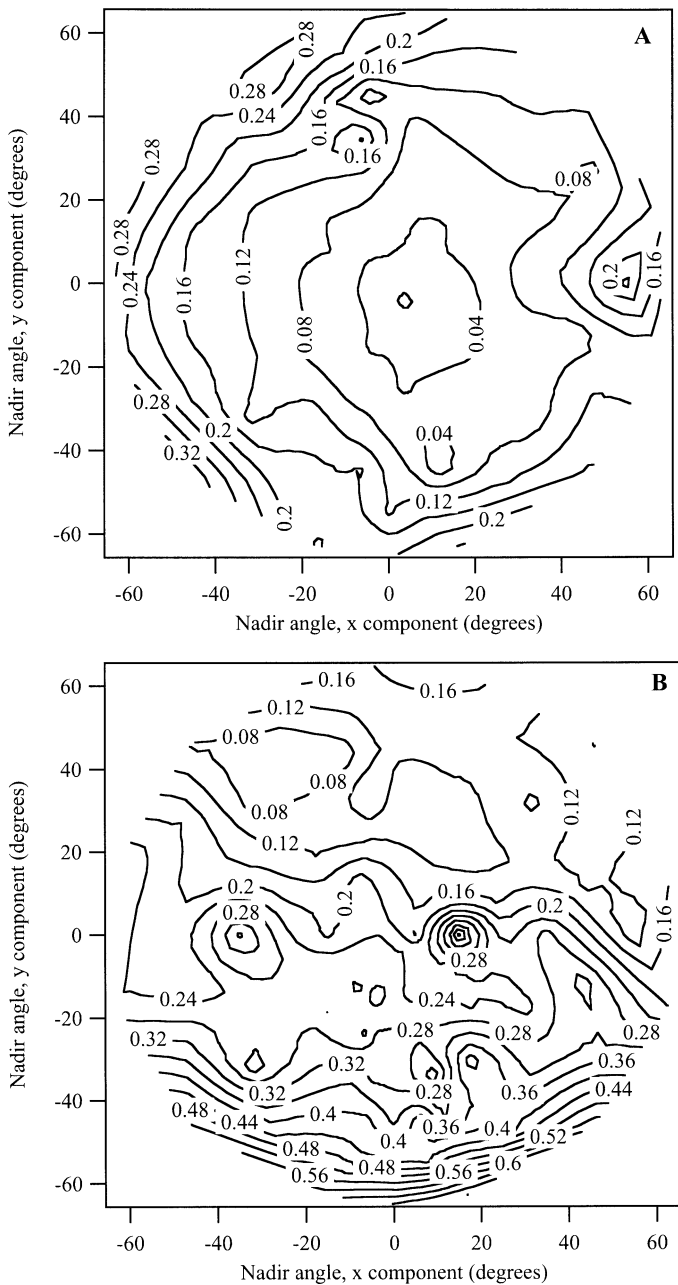


Fig. 4. Normalized standard deviation of the samples used to construct the Norman's Yellow average. (A) $\theta_i = 0^\circ$, (B) $\theta_i = 65^\circ$. Note that this sample was less homogeneous than the Rainbow South case, hence the standard deviation is much higher between samples.

with increasing θ_r . Even so, the decrease to the edge of the measurements is only approximately 0.06, or 25%.

Figure 3B shows the $\text{REFF}(\theta_i, \theta_r, \phi)$ for $\theta_i = 65^\circ$. This also shows a common feature as the grain size increased. The hotspot has increased to a relative increase of a factor of three between $\theta_r = 0^\circ$ and $\theta_r = 65^\circ$, $\phi = 0$. In this sample the increase in reflectance in the specular direction has mostly disappeared.

Figure 4 shows the normalized standard deviation for these two illumination angles. With the larger grain size, and

less homogeneous surface, the standard deviation between the individual measurement samples is larger. One can see that at $\theta_i = 0^\circ$ (Fig. 4A) the standard deviation reaches 30%, while at $\theta_i = 65^\circ$ (Fig. 4B) the standard deviation reaches 60% on the edge. However, in terms of absolute reflectance values this is still less than 0.07. So while there is greater variability between the samples, the absolute magnitude of the variation is not large. For the most part the standard deviation is approximately 10–20% for normal illumination and 20–30% for the illumination at 65° .

Model description—To use in situ BDRF measurements in radiative transfer models it is generally necessary to fit the data to some analytical equation. The important factor for use in the radiative transfer model is that the BRDF model be an accurate representation of the data.

Our starting point for the analytical equation was an earlier model (Walshall et al. 1985), which we refer to as the simple model (WSM):

$$\begin{aligned} \text{REFF}(\theta_i, \theta_r, \phi) = & (C_0 + C_1\theta_i + C_2\theta_i^2) \\ & + (B_0 + B_1\theta_i)\theta_r \cos \phi \\ & + (A_0 + A_1\theta_i + A_2\theta_i^2)\theta_r^2 \end{aligned} \quad (1)$$

This equation, while looking complicated, could be fit in a straightforward fashion. For each incident angle and data set we extracted the data for $\phi = 90^\circ$ and 270° , i.e., 90° from the principal plane (the plane containing the illumination beam and the surface normal). The constants C and A , for each θ_i , are then fit to this data by

$$\text{REFF}(\theta_i, \theta_r, 90^\circ \text{ [or } 270^\circ]) = C + A\theta_r^2 \quad (2)$$

Once C and A are determined, B is found by fitting the data from the rest of the $\text{REFF}(\theta_i, \theta_r, \phi)$ for a specific incident angle. At this point A , B , and C have been determined for each θ_i . Next the A (and B , C) are regressed against θ_i to determine the A_0 , A_1 , and A_2 .

In this equation there is no allowance for a hotspot. Since the hotspot was observed throughout the data set, we added a function to the WSM to account for this. The function chosen was an exponential, dependent on the angle ζ between the incident and viewing direction. ζ is given by

$$\zeta = \arccos(\cos \theta_r \cos \theta_i + \sin \theta_r \sin \theta_i \cos \phi) \quad (3)$$

The difference between the WSM and the measured $\text{REFF}(\theta_i, \theta_r, \phi)$ is calculated for each viewing angle and incident angle. This residual is then fit by the equation

$$\text{REFF}'(\theta_i, \theta_r, \phi) = W_0 + W_1 \exp(-W_2 \zeta) \quad (4)$$

Since a hotspot is only obvious in the data with incident angles $\geq 35^\circ$, this fitting is done for $\theta_i \geq 35^\circ$. Once W_0 , W_1 , and W_2 are found for each θ_i angle, they are fit with a linear equation that varies with θ_i . The final hotspot correction is

$$\begin{aligned} \text{REFF}'(\theta_i, \theta_r, \phi) = & W_{00} + W_{01}\theta_i + (W_{10} + W_{11}\theta_i) \\ & \times \exp(-(W_{20} + W_{21}\theta_i)\zeta) \end{aligned} \quad (5)$$

and should be applied only for $\theta_i \geq 35^\circ$. Finally, for one of our samples the residuals showed a peak in the specular direction that could be fit with another function of the same

Table 2. Model parameters for individual sediment samples.

Parameter	Horseshoe Reef 1	Norman's Yellow	Norman's White	Ooid Shoal	Horseshoe Reef 2	Rainbow South
A_0	-3.95×10^{-5}	-5.44×10^{-5}	-6.32×10^{-5}	-5.53×10^{-6}	-2.23×10^{-5}	8.99×10^{-7}
A_1	5.64×10^{-7}	5.58×10^{-7}	8.73×10^{-7}	2.35×10^{-7}	4.92×10^{-7}	9.84×10^{-8}
A_2	7.80×10^{-9}	1.41×10^{-8}	8.48×10^{-9}	7.92×10^{-9}	5.53×10^{-9}	7.89×10^{-9}
B_0	-1.61×10^{-4}	-5.56×10^{-5}	-1.89×10^{-5}	5.58×10^{-5}	-4.32×10^{-5}	-1.92×10^{-5}
B_1	6.22×10^{-5}	9.51×10^{-5}	9.21×10^{-5}	3.95×10^{-5}	6.94×10^{-5}	4.29×10^{-5}
C_0	9.91×10^{-1}	1.10	1.16	1.03	1.07	1.04
C_1	-5.69×10^{-3}	1.42×10^{-4}	1.89×10^{-3}	3.61×10^{-4}	2.81×10^{-3}	2.76×10^{-3}
C_2	-1.08×10^{-5}	-1.31×10^{-4}	-1.06×10^{-4}	-1.76×10^{-5}	-9.55×10^{-5}	-6.94×10^{-5}
W_{00}	-1.04×10^{-1}	0.00	-3.41×10^{-1}	-1.63×10^{-1}	0.00	-5.51×10^{-2}
W_{01}	1.86×10^{-3}	0.00	5.94×10^{-3}	2.78×10^{-3}	0.00	1.87×10^{-3}
W_{10}	0.00	-8.78×10^{-1}	-8.53×10^{-1}	0.00	-7.66×10^{-1}	0.00
W_{11}	2.24×10^{-2}	4.19×10^{-2}	4.36×10^{-2}	1.22×10^{-2}	3.39×10^{-2}	1.32×10^{-2}
W_{20}	1.37×10^{-2}	3.00×10^{-2}	8.84×10^{-3}	0.00	4.92×10^{-2}	7.76×10^{-2}
W_{21}	6.92×10^{-4}	4.00×10^{-4}	6.96×10^{-4}	6.50×10^{-4}	0.00	0.00
W_{30}	0.00	-7.69×10^{-1}	0.00	0.00	0.00	0.00
W_{31}	0.00	1.96×10^{-2}	0.00	0.00	0.00	0.00
W_{41}	0.00	8.37×10^{-4}	0.00	0.00	0.00	0.00

general shape as the hotspot correction, but in the forward direction.

$$\text{REFF}''(\theta_i, \theta_r, \phi) = (W_{30} + W_{31}\theta_i)\exp(-(W_{41}\theta_i)\gamma) \quad (6)$$

$$\gamma = \arccos[\cos \theta_r \cos \theta_i + \sin \theta_r \sin \theta_i \cos(\phi + 180)] \quad (7)$$

For other samples, while a few seemed to have some specular component, adding this function did not reduce the residuals.

Model application—We applied the model above to sediments from the six sites. When investigating the spectral differences in each sample, we found that if the different colors of the same sample were normalized to some factor, such as $\text{REFF}(\theta_i = 0^\circ, \theta_r = 45^\circ, \phi)$, the fit to the average

of the three normalized colors fit the individual normalized color data as well as if we had fit the model to the colors individually. Thus we normalized each data set by this factor, averaged the normalized color data together, then fit the equation to this data set. Only the blue and red data was used since these were much less noisy than the green data (due to the LED brightness). We chose $\text{REFF}(\theta_i = 0^\circ, \theta_r = 45^\circ, \phi)$ as the normalization parameter because this measurement can be obtained in great spectral detail by other instrumentation (such as the DiveSpec; Mazel 1997).

The resulting model parameters for the samples are shown in Table 2. An example model BRDF is shown in Fig. 5. It is important to have equations that will work for $0^\circ \leq \theta_i, \theta_r \leq 90^\circ$ for most radiative transfer models. With our fitting routines we can apply the equation to 90° for both incident and viewing directions; however, beyond 65° the fit is not validated with data. To show an example of how well this fit works we can look at the residuals, or difference between the model and data, at the specific data points measured. Figure 6 shows these residuals at several incident angles for the Rainbow South sand model. As can be seen, these residuals are small, less than the standard deviation between the measurements. Thus the empirical model does a very good job fitting the measured BRDF. In Fig. 6C it can be seen that the residuals grow in the specular direction. In this case a specular component was not added because we found that adding a specular component tended to increase the residuals elsewhere, thus reducing the overall quality of the fit. There was really only one sample that was helped with the addition of the specular component, and the coefficients for this are shown in Table 2.

Table 3 shows the sample $\text{REFF}(0^\circ, 45^\circ, \phi)$ used to normalize the data to find the above model parameters. To reconstruct the measurements from the model parameters it is necessary to insert the parameters in Table 2 in Eqs. 1, 5, and 6, then multiply by the reflectance factor. In general, for other wavelengths, if $\text{REFF}(0^\circ, 45^\circ, \phi)$ is known, then the BRDF can be determined for that wavelength.

Figure 7 shows the principal plane of the model results

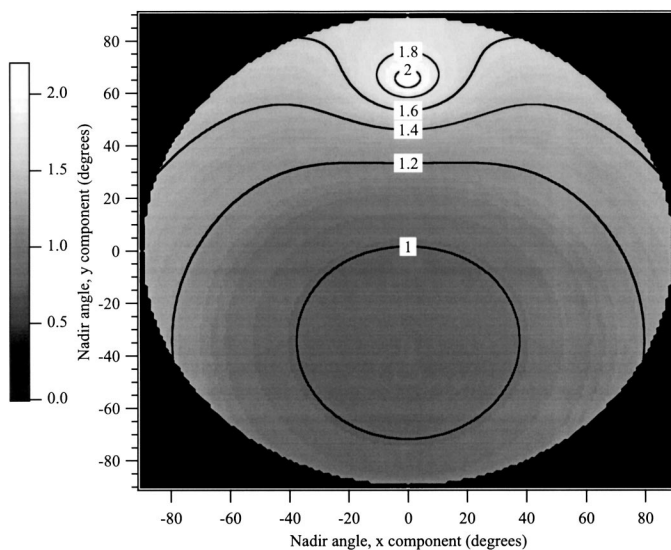


Fig. 5. Model $\text{REFF}(\theta_i, \theta_r, \phi)$ for Rainbow South, $\theta_i = 65^\circ$. Model extends to 90° . Contour lines are every 0.2 in REFF.

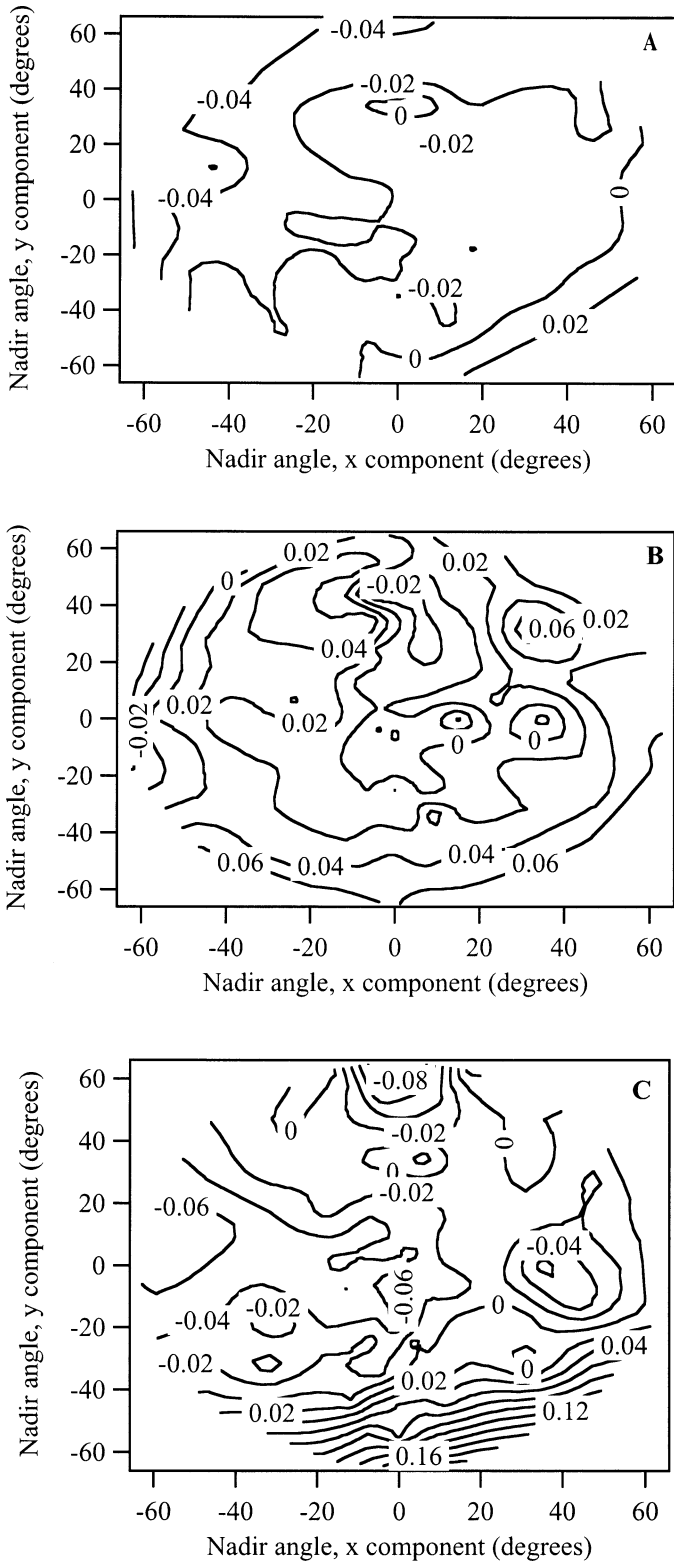


Fig. 6. Deviations (Model REFF(θ_i, θ_r, ϕ) - data REFF(θ_i, θ_r, ϕ)) (A) $\theta_i = 0^\circ$, (B) $\theta_i = 35^\circ$, and (C) $\theta_i = 65^\circ$.

Table 3. REFF($0^\circ, 45^\circ, \phi$) used in sample normalization.

Sample	Blue	Red
Horseshoe Reef 1	0.209	0.418
Norman's Yellow	0.121	0.218
Norman's White	0.299	0.390
Ooid Shoal	0.441	0.560
Horseshoe Reef 2	0.291	0.386
Rainbow South	0.420	0.488

for each sample at $0^\circ, 45^\circ$, and 75° illumination. Several features that appear to be related to the relative grain size in the sample are evident. Starting with 0° illumination (Fig. 7A), the REFF($0^\circ, \theta_r, \phi = 0^\circ$ [and 180°]) for the samples with the smallest grain sizes (Rainbow South and Ooid Shoal) is relatively flat. Contrast this with the samples with the two largest grain sizes (Norman's Yellow and Horseshoe Reef 1) where there is a significant change in REFF with view angle.

As one moves from normal illumination, the hotspot starts to appear. In Fig. 7B,C the data have been normalized to 1.0 at $\theta_r = 0^\circ$. There is a fairly regular progression in the intensity of the hotspot with grain size. The samples with the smallest grain size have the smallest hotspot. The two samples with the largest effective grain size (Horseshoe Reef 1 and Norman's Yellow) have the largest hotspot.

There is no obvious variation of the model parameters (A_0, A_1, A_2 , etc.) with grain size, the obvious physical parameter measured. If one looks at the $C(\theta_i)$ generated from the C_0, C_1 , and C_2 (and similarly the $B(\theta_i)$) there are some relationships that emerge. $C(\theta_i)$ is the factor in the model equation that gives the view direction independent reflectance for a given incident irradiance. $C(\theta_i)$ has a tendency to decrease with increasing θ_i and increasing grain size. $B(\theta_i)$ is the factor that gives an azimuthal dependence on viewing angle to the reflectance. This factor also increases with increasing θ_i and increasing grain size. $A(\theta_i)$, which would be an azimuthally independent variation of reflectance with viewing zenith angle, does not show a regular variation with either incident angle or grain size. The variation of the hotspot parameters with grain size has already been discussed.

Mobley et al. (2003) have shown that for many remote sensing applications, in particular for above water remote sensing, the details of the BRDF are not needed. What is required is the correct irradiance reflectance ($R =$ upwelling irradiance/downwelling irradiance) or albedo. However if the BRDF (or REFF) is not uniform, the albedo will depend on the radiance distribution of the light incident upon the surface. A parameter that describes the albedo, and its variation with nadir angle of the incident collimated irradiance, is the directional albedo, which is defined as

$$R(\theta_i) = \int_{\phi=0^\circ}^{\phi=360^\circ} d\phi \int_{\theta_r=0^\circ}^{\theta_r=\theta_{max}} \text{REFF}(\theta_i, \theta_r, \phi) \cos \theta_r \sin \theta_r d\theta_r \tag{8}$$

Since our data only exist out to $\theta_r = 65^\circ$, the complete $R(\theta_i)$ cannot be calculated without some extrapolation. Fortunately, because of the cosine weighting factor in the definition

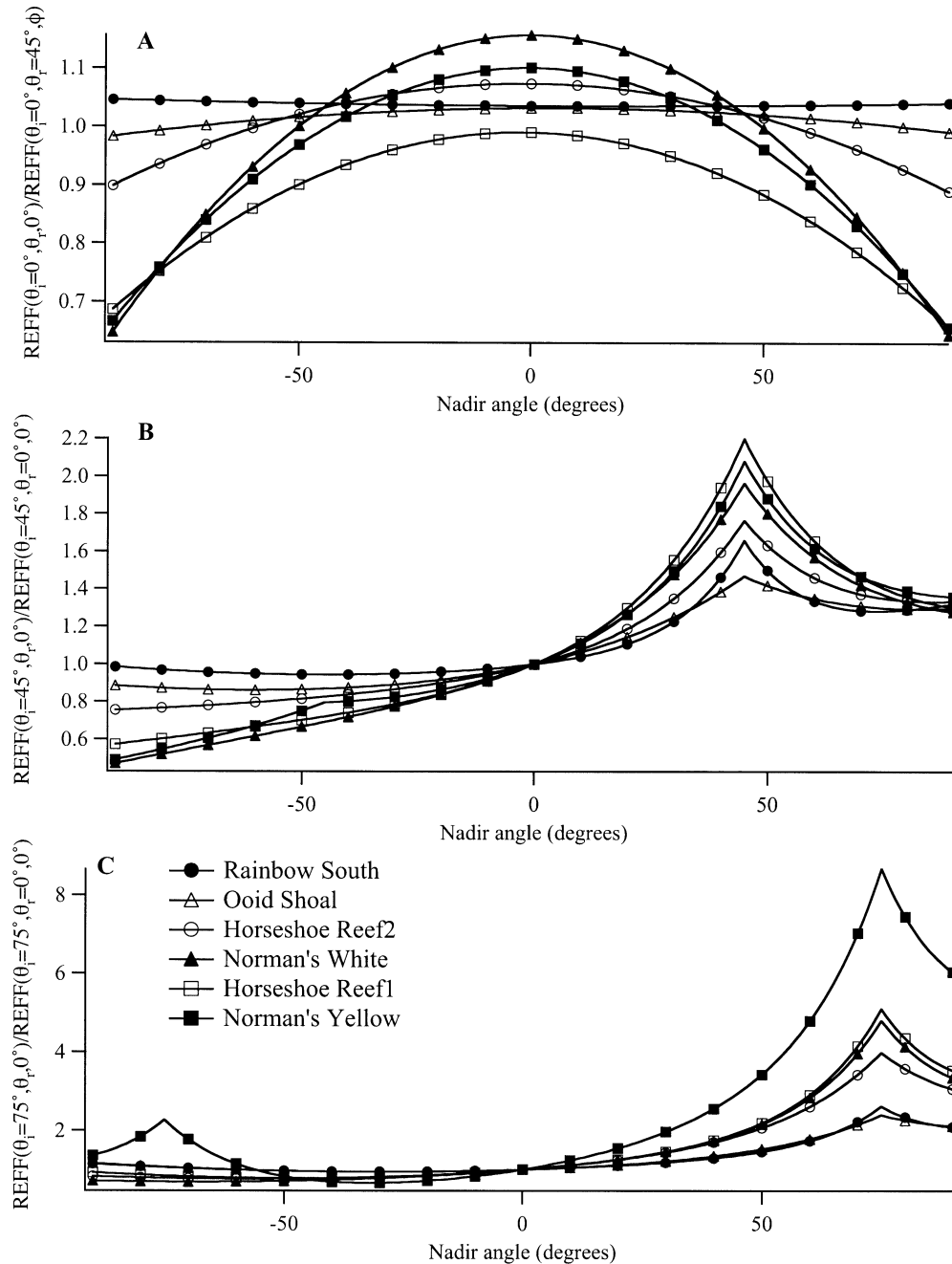


Fig. 7. Comparison of model $\text{REFF}(\theta_i, \theta_r, \phi)/\text{REFF}(\theta_i = 0^\circ, \theta_r = 45^\circ, \phi)$ for the six sites discussed. These data are extracted from the principal plane (plane containing nadir and illumination beam). Illumination angles vary as (A) $\theta_i = 0^\circ$, (B) $\theta_i = 45^\circ$, and (C) $\theta_i = 75^\circ$. (B) and (C) were normalized to one at $\theta_r = 0^\circ$, so they show the growth of the hotspot more clearly.

of upwelling irradiance, the accuracy of the extrapolation is not critical. To see how well the model works to predict $R(\theta_i)$, the two cases we have been concentrating on throughout the paper are shown. Rainbow South is shown in Fig. 8, with Norman's Yellow in Fig. 9. Figures 8 and 9 show $R'(\theta_i)$, where the integral is only out to $\theta_{\max} = 65^\circ$ for both the data and model, and also $R(\theta_i)$ where $\theta_{\max} = 90^\circ$ for both data and model. For the extrapolation of the data, the mean of all the data with $55^\circ \leq \theta_r \leq 65^\circ$ was determined and assigned

to the BRDF above 65° . In Figs. 8 and 9, for each θ_i there are four points, the model and data $R'(\theta_i)$ (which appear lower on the graph), and the model and data $R(\theta_i)$. The data values are calculated by taking each experimental measurement, calculating R and R' , then taking the mean and standard deviation. The error bars are ± 1 SD. In Fig. 8 one can see that the model does a good job of representing both R and R' and that the extrapolation to 90° in θ_r (to compute $R(\theta_i)$) compares well with the model. The largest deviation

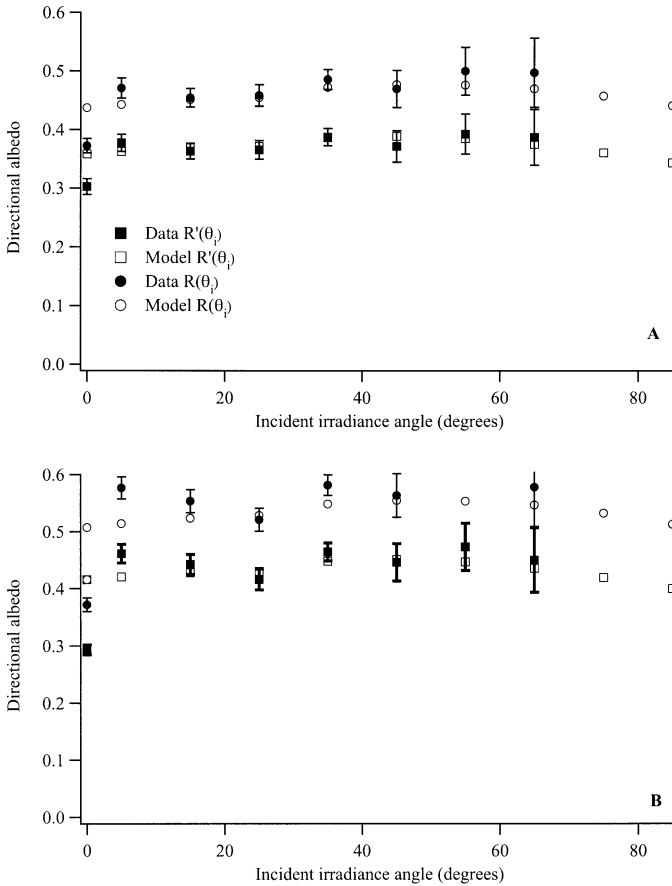


Fig. 8. Rainbow South directional albedo. Shown are both $R(\theta_i)$ (integral extends to 90°) and $R'(\theta_i)$ (integral extends to 65° , the limit of the data). (A) 450 nm, (B) 650 nm. $R(\theta_i)$ and $R'(\theta_i)$ were calculated from each measurement and then averaged. The error bars on data are the standard deviation of the individual $R(\theta_i)$ and $R'(\theta_i)$.

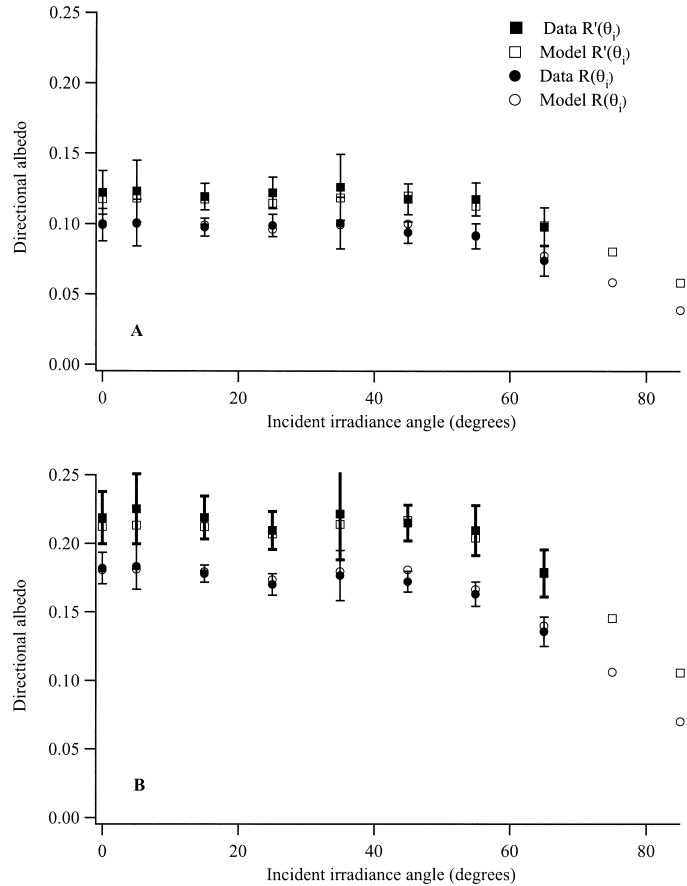


Fig. 9. Norman's Yellow directional albedo. Shown are both $R(\theta_i)$ (integral extends to 90°) and $R'(\theta_i)$ (integral extends to 65° , the limit of the data). Panel (A) is 450 nm, Panel (B) is 650 nm. $R(\theta_i)$ and $R'(\theta_i)$ were calculated from each measurement and then averaged. The error bars on data are the standard deviation of the individual $R(\theta_i)$ and $R'(\theta_i)$.

is at 0° , where the experimental R and R' are suppressed. It is interesting that in this case, the Rainbow South model (and data) has an R that is relatively independent of θ_i .

Contrast Fig. 8 with Fig. 9, which shows the comparison between the model and data for R and R' of Norman's Yellow. Here the agreement between the model and data is also good (within 1 SD). But note that R is now a function of θ_i , decreasing as θ_i increases. This result shows that in spite of having a large hotspot at increased θ_i , the overall irradiance from the surface decreases with increasing θ_i .

To compare the $R(\theta_i)$ for all the samples without including overall magnitude variations, we look at Fig. 10. This is $R(\theta_i)$ for each model normalized with $REFF(0^\circ, 45^\circ, \phi)$, simply the normalization factor used in the models. Here one can find a very nice progression with grain size. Below $\theta_i = 55^\circ$, $R(\theta_i)$ for the four samples with the smallest grain size agrees quite well (grain size $\leq 800 \mu\text{m}$). When $\theta_i > 55^\circ$, $R(\theta_i)$ diverges, with the smallest grain size continuing upward and the other samples decreasing. Interestingly, there is not a significant difference in grain size between Ooid Shoal and Rainbow South, yet they diverge by 20% at $\theta_i = 85^\circ$. The next two largest samples, Norman's White and Horseshoe Reef 2 also fall off with increasing θ_i . The largest two sam-

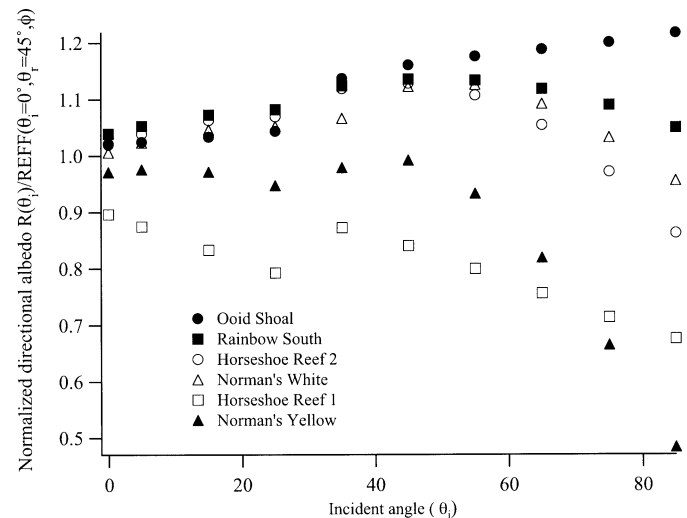


Fig. 10. Normalized directional albedo $[R(\theta_i)/REFF(\theta_i = 0^\circ, \theta_i = 45^\circ, \phi)]$ for each model.

ples have $R(\theta_i)$, which decreases with increasing θ_i . The large variation between $\theta_i = 25^\circ$ and $\theta_i = 35^\circ$ is caused by the addition of the hotspot function at 35° . Because the hotspot is so significant in these large grain size samples, it is difficult to make this transition occur smoothly. The variation at $\theta_i = 0^\circ$ is caused by the differences between the ratio of $R(0^\circ)$, the normal albedo, and $\text{REFF}(0^\circ, 45^\circ, \phi)$ between the different samples. Thus, $\text{REFF}(0^\circ, 45^\circ, \phi)$ is not linearly related to the irradiance reflectance and can vary by at least 10% between samples. This points out the need for additional BRDF measurements since $\text{REFF}(0^\circ, 45^\circ, \phi)$ cannot be used to predict the normally illuminated albedo in general.

In summary, when natural samples are illuminated normal to the surface they appear to be almost Lambertian. As the illumination angle moves from the normal the samples become increasingly non-Lambertian. The deviation from a Lambertian reflector is biggest for the sediments with the larger grain sizes. The dominant feature in the REFF is in the hotspot, or retroreflection, direction. The hotspot increases with sediment size and increasing illumination angles.

The empirical model presented for each sediment type that represents the data within a standard deviation of the sample variation. This model is well behaved at angles out to 90° ; thus it can be used in radiative transfer models. With this model, a realistic bottom reflectance can be added to improve the light field predictions in shallow waters.

In this paper, we have not addressed the physical reasons for why the REFF appears as it does. The model we have chosen does not lend itself to a physical interpretation of the parameters. In fact there is much discussion in the literature about how the BRDF is related to the individual particle optics (Hapke 1999; Mischenko and Macke 1997) or how radiative transfer works in a densely packed medium (Goedecke 1977). The preliminary route to such a physically based BRDF should involve careful laboratory measurements of the REFF of simple systems (such as regular spheres), then working toward a predictive model for the REFF. We are currently working on this. Until a predictive model of the REFF is developed, these measurements cover a range of sediment types and sizes in the natural environ-

ment; thus they could be applied in other environments where the sediment has similar physical attributes.

References

- CARDER, K. L., AND OTHERS. 2003. Illumination and turbidity effects on observing faceted bottom elements with uniform Lambertian albedos. *Limnol. Oceanogr.* **48**: 355–363.
- GOEDECKE, G. H. 1977. Radiative transfer in closely packed media. *J. Opt. Soc. Am.* **67**: 1339–1348.
- HAPKE, B. 1993. *Theory of reflectance and emittance spectroscopy*. Cambridge Univ. Press.
- . 1999. Scattering and diffraction of light by particles in planetary regoliths. *J. Quant. Spectrosc. Radiat. Transfer* **61**: 565–581.
- MARITORENA, S., A. MOREL, AND B. GENTILI. 1994. Diffuse reflectance of oceanic shallow waters: Influence of water depth and bottom albedo. *Limnol. Oceanogr.* **39**: 1689–1703.
- MAZEL, C. H. 1997. Diver-operated instrument for in situ measurement of spectral fluorescence and reflectance of benthic marine organisms and substrates. *Opt. Eng.* **36**: 2612–2617.
- MCGUCKIN, B. T., D. A. HANER, AND R. T. MENZIES. 1997. Multi-angle imaging spectroradiometer: Optical characterization of the calibration panels. *Appl. Opt.* **36**: 7016–7022.
- MISCHENKO, M. I., AND A. MACKE. 1997. Asymmetry parameters of the phase function for isolated and densely packed spherical particles with multiple internal inclusions in geometric optics limit. *J. Quant. Spectrosc. Radiat. Transfer* **57**: 767–794.
- MOBLEY, C. D., AND L. K. SUNDMAN. 2003. Effects of optically shallow bottoms on upwelling radiances: Inhomogeneous and sloping bottoms. *Limnol. Oceanogr.* **48**: 329–336.
- , H. ZHANG, AND K. J. VOSS. 2003. Effects of optically shallow bottoms on upwelling radiances: Bidirectional reflectance distribution function effects. *Limnol. Oceanogr.* **48**: 337–345.
- VOSS, K. J., A. CHAPIN, M. MONTI, AND H. ZHANG. 2000. An instrument to measure the bi-directional reflectance distribution function (BRDF) of surfaces. *Appl. Opt.* **39**: 6197–6206.
- WALTHALL, C. L., J. M. NORMAN, J. M. WELLES, G. CAMPBELL, AND B. L. BLAD. 1985. Simple equation to approximate the bi-directional reflectance from vegetative canopies and bare soil surfaces. *Appl. Opt.* **24**: 383–387.
- ZANEVELD, J. R. V., AND E. BOSS. 2003. The influence of bottom morphology on reflectance: Theory and two-dimensional geometry model. *Limnol. Oceanogr.* **48**: 374–379.

Received: 14 September 2001

Accepted: 30 April 2002

Amended: 29 May 2002